

1 **Retrieval of cloud fraction using random forest based on FY4A AGRI**  
2 **observations.**

3 Jinyi Xia<sup>1</sup> Li Guan<sup>1</sup>

4 <sup>1</sup>China Meteorological Administration Aerosol-Cloud and Precipitation Key  
5 Laboratory, Nanjing University of Information Science and Technology, Nanjing  
6 210044, China

7 Correspondence to: Li Guan [liguan@nuist.edu.cn](mailto:liguan@nuist.edu.cn)

8  
9 **Abstract**

10 Cloud fraction as a vital component of meteorological satellite products plays an  
11 essential role in environmental monitoring, disaster detection, climate analysis, and  
12 other research areas. A **random forest** machine learning algorithm is used in this paper  
13 to retrieve the cloud fraction of AGRI (Advanced Geosynchronous Radiation Imager)  
14 onboard FY-4A satellite based on its full-disc level-1 radiance observation. Corrections  
15 has been made subsequently to the retrieved cloud fraction in areas where solar glint  
16 occurs using a correction curve fitted with sun-glint angle as weight. The algorithm  
17 includes two steps: the cloud detection is conducted firstly for each AGRI field of view  
18 to identify whether it is clear sky, partly cloudy or overcast within the observation field.  
19 Then the cloud fraction is retrieved for the scene identified as partly cloudy. The 2B-  
20 CLDCLASS-LIDAR cloud fraction product from Cloudsat& CALIPSO active remote  
21 sensing satellite is employed as the truth to assess the accuracy of the retrieval algorithm.

删除了: Using machine learning algorithm to retrieve cloud fraction based on FY-4A AGRI observations

删除了: long short-term memory (LSTM)

删除了: ia

删除了: cloud coverage

27 Comparison with the operational AGRI level 2 cloud fraction product is also conducted  
28 at the same time. During daytime, the probability of detection (POD) for clear sky,  
29 partly cloudy, and overcast scenes in the operational cloud detection product were  
30 0.5359, 0.7041, and 0.7826, respectively. The POD for cloud detection using the  
31 random forest algorithm were 0.6984, 0.8971, and 0.8613. While the operational  
32 product often misclassified clear sky scenes as cloudy, the random forest algorithm  
33 improved the discrimination of clear sky scenes. For partly cloudy scenes, the mean  
34 error (ME) and root-mean-square error (RMSE) of the operational product were 0.2374  
35 and 0.3269. The random forest algorithm exhibited lower ME (0.1457) and RMSE  
36 (0.2022) than the operational product. The large reflectance in the sun-glint region  
37 resulted in significant cloud fraction retrieval errors using the random forest algorithm.  
38 However, after applying the correction, the accuracy of cloud cover retrieval in this  
39 region gets greatly improved. During nighttime, the random forest model demonstrated  
40 improved POD for clear sky and partly cloudy scenes compared to the operational  
41 product, while maintaining a similar POD value for overcast scenes and a lower FAR.  
42 For partly cloudy scenes at night, the operational product exhibited a positive mean  
43 error, indicating an overestimation of cloud cover, whereas the random forest model  
44 showed a negative mean error, indicating an underestimation of cloud cover. The  
45 random forest model also exhibited a lower RMSE compared to the operational product.  
46 **Key words:** Cloud detection, cloud fraction, FY-4A AGRI, Random Forest.

删除了: official

删除了: LSTM

删除了: 8294

删除了: 7223

删除了: 8435

删除了: LSTM

删除了: , albeit with a higher false alarm rate compared to the operational product

删除了: LSTM

删除了: 1134

删除了: 1897

删除了: LSTM

删除了: LSTM

删除了: false alarm rate

删除了: LSTM

删除了: LSTM

删除了: LSTM neural network

## 64 Introduction

65 Clouds occupy a significant proportion within satellite remote sensing data  
66 acquired for Earth observation. According to the statistics from the International  
67 Satellite Cloud Climatology Project (ISCCP), the annual average global cloud coverage  
68 within satellite remote sensing data is around 66% with even higher cloud coverage in  
69 specific regions (such as the tropics) (Zhang, et al., 2004). The impact of clouds on the  
70 radiation balance of the Earth's atmospheric system is influenced by the optical  
71 properties of clouds. Cloud detection, as a vital component of remote sensing image  
72 data processing, is considered a critical step for the subsequent identification, analysis,  
73 and interpretation of remote sensing images. Therefore, accurately determining cloud  
74 coverage is essential in various research domains, such as environmental monitoring,  
75 disaster surveillance and climate analysis.

76 Fengyun-4A (FY-4A) is a comprehensive atmospheric observation satellite  
77 launched by China in 2016. The uploaded AGRI (Advanced Geosynchronous Radiation  
78 Imager) has 14 channels and captures full-disk observation every 15 minutes. In  
79 addition to observing clouds, water vapor, vegetation and the Earth's surface, it also  
80 possesses the capability to capture aerosols and snow. Moreover, it can clearly  
81 distinguish different phases and particle size of clouds and obtain high- to mid-level  
82 water vapor content. It is particularly suitable for cloud detection due to its  
83 simultaneous use of visible, near-infrared, and long-wave infrared channels for

删除了:

删除了: determined

86 observation with 4km spatial resolution.

删除了: high

87 Numerous cloud detection algorithms have been provided based on observations  
88 from satellite-borne imagers. The threshold method has been widely employed by  
89 researchers, including the early ISCCP (International Satellite Cloud Climatology  
90 Project) method (Rossow, 1993) and the proposed threshold methods based on different  
91 spectral features or underlying surfaces (Kegelmeyer, 1994; Solvsteen, 1995; Baum and  
92 Trepte, 1996). However, there is a significant subjectivity in selection of thresholds  
93 whether it is the single and fixed threshold in the early days, multiple thresholds,  
94 dynamic thresholds, or adaptive thresholds. The selection of thresholds is influenced  
95 by season and climate. Surface reflectance varies significantly between different  
96 seasons, such as increased reflectance from snow in winter and vegetation flourishing  
97 in summer affecting reflectance. As a result, changes in surface features during different  
98 seasons lead to variations in the distribution of grayscale values in images, requiring  
99 adjustments to thresholds based on seasonal characteristics. Climate conditions like  
100 cloud cover, atmospheric humidity, etc., impact the distinguishability of clouds and  
101 other features. For instance, in humid or cloudy climates, the reflectance of the surface  
102 and clouds may be similar, necessitating stricter thresholds for differentiation.  
103 Therefore, climate conditions also influence threshold selection.

删除了: encompassing

删除了: Kegelmeyer (1994) used a straightforward cloud pixel as threshold for cloud detection with Whole Sky Imaging Cameras. Solvsteen (1995) distinguished cold water pixels and cloud pixels by analyzing the correlation between different channels based on AVHRR (Advanced Very High Resolution Radiometer) images. A grouping threshold method based on AVHRR images has been developed by Baum and Trepte (1996) to classify scenes as clouds, fires, smoke or snow. LI and Zhang (2006) proposed a multispectral integrated cloud detection algorithm based on the characteristics of MODIS instrument channels and the spectral characteristics of different objects (clouds, snow, land, etc.). Zhang et al. (2020) used a multi-temporal cloud detection method based on FY-4A AGRI data to identify observations on the Qinghai-Tibet Plateau.

删除了: These thresholds are highly influenced by factors such as season and climate.

104 The other category of cloud detection algorithms is based on statistical probability  
105 theory. For example the principal component discriminant analysis and quadratic

删除了: the

删除了: Such as

106 discriminant analysis methods were used to SEVIRI (Spinning Enhanced Visible and

128 Infrared Imager) cloud detection (Amato et al., 2008). The cloud detection algorithm  
129 for Thermal Infrared (TIR) sensor was based on the Bayesian theory of total probability  
130 (Merchant et al., 2010) and the naive Bayes algorithm for AGRI (Qu , et al., 2022). The  
131 unsupervised clustering cloud detection algorithms for MERIS (Medium Resolution  
132 Imaging Spectrometer) (GomezChova , et al., 2007) and the fuzzy C-means clustering  
133 algorithms for MODIS (Pan, et al., 2009) all have achieved high accuracy in cloud  
134 detection.

135 More and more machine learning algorithms are being utilized by researchers in  
136 cloud detection studies with the development of machine learning. For instance, the  
137 probabilistic neural networks, especially radial basis function networks was used for  
138 AVHRR cloud detection (Zhang, et al., 2001). The utilization of convolutional neural  
139 network methods (Hu, et al., 2020) offers important perspectives for cloud detection  
140 research.

141 Currently, there is limited research literature on cloud detection and cloud fraction  
142 retrieval algorithms for FY-4A/4B AGRI. The operational cloud fraction product of FY-  
143 4A AGRI utilized a threshold method with 4 km spatial resolution. Differences in  
144 climatic and environmental factors lead to varying albedo and brightness temperature  
145 observations for the instrument at different times and locations. Therefore, the choice  
146 of thresholds is easily influenced by factors such as season, latitude and land surface  
147 type (Gao and Jing, 2019). Using multiple sets of thresholds for discrimination would  
148 significantly slow down the cloud detection process. Moreover, most algorithms focus

149 solely on cloud detection, which classified the observed scenes into cloud or clear-sky  
150 without providing the specific cloud fraction information for the scenes. The use of  
151 active remote sensing instruments carried by Cloudsat & Calypso is not influenced by  
152 thresholds when retrieving cloud fraction, enabling a more accurate cloud fraction  
153 retrieval. However, due to Cloudsat & Calypso being polar-orbiting satellites, the cloud  
154 fraction over the full disk cannot be obtained. Utilizing the Cloudsat & Calypso Level  
155 2 product 2B-CLDCLASS-LIDAR as the reference truth, a random forest model trained  
156 based on FY4A AGRI full disk radiation data can address the shortcomings of threshold  
157 methods and achieve a high accuracy of cloud fraction over the full disk. Moreover, the  
158 parallel processing during training, randomness in feature selection, and random  
159 sampling of samples in random forest make it have a faster training speed compared to  
160 other algorithms with similar performance.

161 In summary, a random forest machine learning algorithm for cloud fraction  
162 retrieval was established using level-1 radiation observations from FY-4A AGRI full-  
163 disk scanning in this paper. The cloud fraction of the level-2 product 2B-CLDCLASS-  
164 LIDAR from Cloudsat&CALIPSO was used as the reference label. The retrievals were  
165 compared against with the cloud fraction of 2B-CLDCLASS-LIDAR and the AGRI  
166 operational products to verify the algorithm accuracy.

删除了: The full disk data contains data for different latitudes, different seasons, and different surface types. The random forest model trained based on full disk data can solve the shortcomings of the threshold method itself. In addition, the characteristics of random forest in the training process, such as parallelization processing, randomness of feature selection and random sampling of samples, make it have a faster training speed than other algorithms

删除了: .

删除了: LSTM (Long Short-Term Memory)

## 177 **1 Research Data and Preprocessing**

### 178 **1.1 FY-4A data**

179 FY-4A was successfully launched on December 11, 2016. Starting from May 25, 2017,  
180 FY-4A drifted to a position near the main business location of the Fengyun  
181 geostationary satellite at 104.7 degrees east longitude on the equator. Its successful  
182 launch marked the beginning of a new era for China's next-generation geostationary  
183 meteorological satellites as an advanced comprehensive atmospheric observation  
184 satellite. The Advanced Geosynchronous Radiation Imager (AGRI), one of the main  
185 payloads of the Fengyun-4 series geostationary meteorological satellites, can perform  
186 large-disk scans and rapid regional scans at a minute level. It has 14 observation  
187 channels in total with the main task of acquiring cloud images. The channel parameters  
188 and main uses of AGRI are detailed in Table 1  
189 (<https://www.nsmc.org.cn/nsmc/cn/instrument/AGRI.html>). FY-4A AGRI data was  
190 downloaded from the official website of the China national satellite meteorological  
191 center (<http://satellite.nsmc.org.cn>), including level-1 full disk radiation observation  
192 data preprocessed through quality control, geolocation and radiation calibration as well  
193 as level-2 cloud fraction product (CFR). The spatial resolution of these data is all 4 km  
194 at nadir and the temporal resolution is 15 minutes.

删除了: total

195 **Table 1** FY-4A AGRI channel parameters

Channel Number	Band Range / $\mu\text{m}$	Central Wavelength / $\mu\text{m}$	Spatial resolution/km	Main Applications
1	0.45 ~ 0.49	0.47	1	clouds, dust, aerosols

2	0.55 ~ 0.75	0.65	0.5	clouds, sand dust, snow
3	0.75 ~ 0.90	0.825	1	vegetation
4	1.36 ~ 1.39	1.375	2	cirrus
5	1.58 ~ 1.64	1.61	2	clouds、 snow
6	2.10 ~ 2.35	2.225	2	cirrus、 aerosols
7	3.50 ~ 4.00	3.75H	2	fire point, the intense solar reflection signal
8	3.50 ~ 4.00	3.75L	4	low clouds, fog
9	5.80 ~ 6.70	6.25	4	upper-level water vapor
10	6.90 ~ 7.30	7.1	4	mid-level water vapor
11	8.00 ~ 9.00	8.5	4	subsurface water vapor
12	10.30 ~ 11.30	10.8	4	surface and cloud-top temperatures
13	11.5 0~ 12.50	12.0	4	surface and cloud-top temperatures
14	13.2 ~ 13.8	13.5	4	cloud-top height

197

## 198 1.2 CloudSat & Calipso Cloud Product

199 CALIPSO (Cloud-Aerosol Lidar and Infrared Pathfinder Satellite Observations)  
200 is a satellite jointly launched by NASA and CNES (the French National Center for  
201 Space Studies) in 2006. It is a member of the A-Train satellite observation system.  
202 CALIPSO is equipped with three payloads, among which CALIOP (the Cloud and  
203 Aerosol Lidar with Orthogonal Polarization) is a primary observational instrument.  
204 Observing with dual wavelengths (532 nm and 1064 nm) CALIOP can provide high-  
205 resolution vertical profiles of clouds and aerosols with 30 m vertical resolution. As the  
206 first satellite designed to observe global cloud characteristics in a sun-synchronous orbit  
207 CloudSat is also among NASA's A-Train series satellites. The CPR (Cloud Profile  
208 Radar) installed on it operates at 94 GHz millimeter-wave and is capable of detecting



209 the vertical structure of clouds and providing vertical profiles of cloud parameters. The  
210 scanning wavelengths of CPR and CALIOP are different. CALIOP is capable of  
211 observing the top of mid-to-high level clouds, whereas CPR can penetrate optically  
212 thick clouds. Combining the strengths of these two instruments enables the acquisition  
213 of precise and detailed information on cloud layers and cloud fraction.

214 The joint level 2 product 2B-CLDCLASS-LIDAR is mainly utilizing in this study.  
215 It provides the cloud fraction at different heights with horizontal resolution 2.5 km  
216 (along-track) × 1.4 km (cross-track) through combining the observations from CPR and

217 CALIOP. Since the two instruments have different spatial domain such as vertical  
218 resolution, spatial resolution and spatial frequency, the spatial domain of the output  
219 products is defined in terms of the spatial grid of the CPR. In the algorithm, the cloud  
220 fraction is calculated using a weighted scheme based on the spatial probability of  
221 overlap between the radar and lidar observations. The calculation of the lidar cloud  
222 fraction within a radar footprint is represented by the equation 1(Mace, G. G., et al,  
223 2007):

$$224 \quad C_l = \frac{\sum_{i=1}^{\# \text{ of lidar obs}} w_i \delta_i}{\sum_{i=1}^{\# \text{ of lidar obs}} w_i} \quad (1)$$

225 Where:

226  $C_l$  represents the lidar cloud fraction within a radar footprint.

227  $w_i$  is the spatial probability of overlap for a particular lidar observation.

228  $\delta_i$  indicates the lidar hydrometeor occurrence, where a value of 1 signifies the  
229 presence of hydrometeor and 0 indicates the absence.

删除了: (Zhen, et al., 2018)

231 i counts the lidar profile in a specific radar observational domain.  
232 This calculation considers the contributions of multiple lidar observations within  
233 a radar resolution volume to determine the cloud fraction within that volume.The  
234 CloudSat product manual (Wang, 2019) can be referred for more detailed information  
235 on 2B-CLDCLASS-LIDAR. The data used is available to download from the ICARE  
236 data and services center ([https://www.icare.univ-lille.fr/data-access/data-archive-](https://www.icare.univ-lille.fr/data-access/data-archive-access/)  
237 [access/](https://www.icare.univ-lille.fr/data-access/data-archive-access/)).

删除了: for

### 238 1.3 Establishment of Training Data

239 The crucial aspect of establishing a training data in machine learning algorithms  
240 is how to obtain the cloud fraction values (ground truth) as labels. The error in cloud  
241 fraction retrieved solely from passive remote sensing instruments is significant. Using  
242 active remote sensing data can provide more accurate cloud fraction information in the  
243 vertical direction. Therefore, the spatiotemporally matched 2B-CLDCLASS-LIDAR  
244 cloud fraction are utilized as output labels in this paper.

245 The FY-4A AGRI and 2B-CLDCLASS-LIDAR data with a spatial difference  
246 between fields of view within 1.5 km and a time difference within 15 minutes are  
247 spatiotemporal matched. To make the 2B-CLDCLASS-LIDAR cloud fraction data  
248 collocated within AGRI pixels more effective, at least two 2B-CLDCLASS-LIDAR  
249 pixels are required within each AGRI field of view. The cloud fraction average of these  
250 pixels is used as the cloud fraction for that AGRI pixel.

删除了: distance

253 Cloud detection and cloud fraction label generation for 2B-CLDCLASS-LIDAR  
254 are as follows. There may be multiple layers of clouds in each field of view. If there is  
255 at least one layer cloud with cloud fraction of 1 in the 2B-CLDCLASS-LIDAR profile,  
256 then the scene is labeled as overcast with a cloud fraction of 1. If all layers in the profile  
257 are cloud-free, the scene is labeled as clear sky. The scene between the above two  
258 situations is labeled as partly cloudy and the cloud fraction is the average of cloud  
259 fractions at different layers.

260 The algorithm includes two steps: the cloud detection is conducted firstly for each  
261 AGRI field of view to identify whether it is clear sky, partly cloudy or overcast within  
262 the observation field. Then the cloud fraction is retrieved for the scene identified as  
263 partly cloudy. So the training data include A dataset used for cloud detection and B  
264 dataset for cloud fraction retrieval. The input variables in A dataset are the FY-4A  
265 AGRI level-1 radiative observations from 14 channels and the output variable is the  
266 temporally and spatially matched 2B-CLDCLASS-LIDAR cloud detection label. The  
267 output is categorized into three types: overcast, partly cloudy and clear sky with values  
268 1, 2 and 3 respectively. To ensure diversity and representativeness of the samples, the  
269 three conditions of overcast, partly cloudy, and clear sky each account for one-third of  
270 the sample size in dataset A. Regarding the samples for partly cloudy type in dataset A,  
271 the collocated 2B-CLDCLASS-LIDAR cloud fraction products serve as output labels  
272 for cloud fraction retrieval model B. The input of training dataset B remains the FY-4A  
273 AGRI level-1 radiative observations.

删除了: ia

删除了: cloud coverage

276 Due to the instrument's limited lifespan, only 2B-CLDCLASS-LIDAR data up to  
277 August 2019 can be obtained. Additionally, the latitude range for a single observation  
278 of FY-4A AGRI is -83.3~83.3. Within this latitude range, data from different seasons,  
279 climates, and surface types are included. In the training samples matched in space-time  
280 with 2B-CLDCLASS-LIDAR, seasons and climates vary with latitude. Therefore, there  
281 is no need to include data from a larger time range as training samples. The FY-4A  
282 AGRI observations and 2B-CLDLASS-LIDAR matched in time and space in May 2019  
283 are used as training samples to build the algorithm model. The paired samples of whole  
284 June 2019 are served as the testing samples to assess the model's retrieval accuracy. The  
285 number of training samples in May are 12,420 for dataset A and 4140 for B. Testing  
286 samples in June are 15,459 for A and 5,153 for B.

287 Although the retrieval model was trained and tested using 2019 data, the algorithm  
288 was also applied to real-time observations of FY-4A and FY-4B AGRI in 2023 to verify  
289 its universality.

290

## 291 **2. Random Forest Algorithm**

292 The random forest algorithm integrates multiple trees based on the Bagging idea  
293 of ensemble learning, with the basic element being the decision tree (Breiman, 1999).  
294 When building a decision tree, N sets of independent and dependent variables are

删除了: Due to the lifespan of the instrument only 2B-CLDCLASS-LIDAR data before July 2019 can be obtained.

删除了: So, t

删除了: Long Short-Term Memory (LSTM)

299 randomly sampled with replacement from the original training samples to create a new  
300 training sample set; m variables are randomly sampled without replacement from all  
301 independent variables, the dependent variable data is split into two parts using the  
302 selected variables, and the purity of the subsets is calculated for each split method. The  
303 variable utilized by the split method with the highest purity is used to partition the data,  
304 completing the decision at that node. This process of binary splitting continues to grow  
305 the decision tree until stopping criteria are met, completing the construction of a single  
306 decision tree. These steps are repeated Ntree times to build a random forest model  
307 consisting of Ntree decision trees (Quesada-Ruiz et al., 2022). Random Forest adopts  
308 ensemble algorithms, with the advantage of high accuracy. It can handle both discrete  
309 and continuous data, without the need for normalization, making it more efficient  
310 compared to other algorithms.

311 In this study, when using the trained model for prediction, observations from 14  
312 channels are inputted into the model. Each decision tree independently predicts the  
313 outcome, with a majority vote determining the final classification category of overcast,  
314 partly cloudy, or clear sky. For regression tree models, the average of all tree outputs is  
315 taken as the final output, representing the specific cloud fraction.

316 Two crucial parameters in the random forest model are the node splitting  
317 frequency Mtry and the number of decision trees Ntree, which directly impact the  
318 model's performance. A high Mtry value can increase model complexity, leading to  
319 overfitting; conversely, a low Mtry can result in a model that is too simple and underfits

320 the data. A small Ntree value can result in underfitting, while a large Ntree significantly  
 321 increases computational load, with minimal performance improvement beyond a  
 322 certain threshold. Typically, setting Mtry to  $\sqrt{M}$ , where M represents the number of  
 323 input variables, results in the lowest model error. For daytime models, M is 14, while  
 324 for nighttime, it is 8. Mtry is set at 3 for daytime cloud detection and cloud fraction  
 325 retrieval models, and at 2 for nighttime models. When determining the size of Ntree, it  
 326 is necessary to do so through cross-validation. The dataset is divided into training and  
 327 validation sets, using a different number of trees in each training iteration, and then  
 328 evaluating the model's performance on the validation set. The best number of trees is  
 329 selected by comparing the performance of the model with different numbers of trees.  
 330 Both daytime and nighttime cloud detection models are configured with Ntree set to  
 331 380, while cloud fraction retrieval models have Ntree set to 300 for both daytime and  
 332 nighttime scenarios.

### 333 3. Results and Analysis

334 To assess the accuracy and stability of the retrieval model, two types of validation  
 335 methods are utilized. One way involves a direct comparison from images, qualitatively  
 336 comparing the model's retrieval results and official cloud fraction products with AGRI  
 337 observed cloud images. Another way is quantitative comparison using 2B-  
 338 CLDCLASS-LIDAR as the true value. Four quantitative parameters, including

删除了: LSTM is an improved algorithm based on RNN (Recurrent Neural Network) with the ability to retain long-term memory. and demonstrates improved performance in longer sequences data comparing to ordinary RNNs (Sarker, 2001). It can effectively address the challenges of gradient explosion and gradient vanishing over time in models., LSTM network has been extensively applied in diverse domains owing to its distinctive features, such as meteorology and environmental prediction and so on (Bao, et al., 2024; Bai and Shen. 2019). The structure of the LSTM unit is depicted in Figure 1. The update and transmission of historical information is facilitated through the internal control of three states: the Forget Gate, the Input Gate and the Output Gate. The pertinent mathematical expressions are:

$$f_t = \sigma(W_f^T \times [h_{t-1}, x_t] + b_f) \quad (1)$$

where  $f_t$  denotes the output of the Forget Gate,  $\sigma$  signifies the Sigmoid activation function;  $W_f^T$  and  $b_f$  correspond to the weight and bias of the Forget Gate, respectively,  $x_t$  stands for the current input,  $h_{t-1}$  represents the output from the previous time step.

$$i_t = \sigma(W_i^T \times [h_{t-1}, x_t] + b_i) \quad (2)$$

where  $i_t$  represents the information updated after  $\sigma$  activation,  $W_i^T$  and  $b_i$  denote the weight and bias, respectively.

$$\hat{C}_t = \sigma(W_c^T \times [h_{t-1}, x_t] + b_c) \quad (3)$$

$\hat{C}_t$  signifies the information updated after tanh activation,  $W_c^T$  and  $b_c$  denote the weight and bias, respectively.

$$C_t = f_t \times C_{t-1} + i_t \times \hat{C}_t \quad (4)$$

$C_t$  is the current information of the LSTM structure,  $C_{t-1}$  denotes the information of the LSTM structure from the previous time step.

$$O_t = \sigma(W_o^T \times [h_{t-1}, x_t] + b_o) \quad (5)$$

$O_t$  is the current output information,  $W_o^T$  and  $b_o$  denote the weight and bias, respectively.

$$h_t = o_t \times \tanh(C_t) \quad (6)$$

422 possibility of detection (POD), false alarm rate (FAR), mean error (ME), and root mean  
423 square error (RMSE) are introduced. The POD is calculated using the formula  
424  $POD = TP / (TP + FN)$ , and the FAR is calculated using the formula  $FAR = FP / (TP + FP)$ .  
425 Taking the overcast scenes as an example, TP represents the number of correctly  
426 identified overcast, FN represents the number of overcast scenes wrongly identified as  
427 partly cloudy or clear sky, and FP represents the number of clear sky or partly cloudy  
428 scenes wrongly identified as overcast. The ME (mean error) and RMSE (root mean  
429 square error) are utilized to assess the accuracy of the random forest cloud fraction  
430 model in retrieving cloud fractions for partly cloudy scenes.

删除了: false alarm rate

删除了: LSTM

### 431 3.1 Objective Analysis of Cloud Fraction Retrievals

432 The test samples from dataset A (i.e., June data) are used to perform cloud  
433 detection experiments based on the cloud detection model mentioned above. The  
434 temporally and spatially matched 2B CLDCLASS-LIDAR cloud mask products are  
435 used as reference to evaluate the accuracy of cloud detection. The POD and FAR for  
436 different view field classifications are shown in Table 2. Columns 2 and 4 represent the  
437 operational cloud detection products for daytime and nighttime respectively, for the  
438 same time and pixel. Columns 3 and 5 represent the random forest cloud detection  
439 results for daytime and nighttime respectively. The table indicates that during daytime,  
440 operational cloud detection products have a relatively low possibility of detection for  
441 clear sky view fields. However, the random forest model increases the possibility of

删除了: LSTM

删除了: LSTM

446 detection for clear sky from 0.54 to 0.70. Moreover, for partly cloudy and overcast view  
 447 fields, the POD is higher than operational cloud detection products. During nighttime,  
 448 compared to operational cloud detection products, the random forest model increases  
 449 the POD for clear sky from 0.51 to 0.67, with higher POD for partly cloudy view fields  
 450 compared to the operational products, while the POD for overcast view fields is lower.  
 451 During the day, the Operational product has a lower FAR for clear sky compared to the  
 452 random forest model, while the random forest model has a lower FAR for partly cloudy  
 453 and overcast conditions compared to the operational product. At night, the random  
 454 forest model significantly reduces the FAR for overcast conditions compared to the  
 455 Operational product.

456 **Table 2** POD and FAR of Cloud Detection

	Sky Classification	Daytime Operational Product	Daytime RF Results	Nighttime Operational Product	Nighttime RF Results
POD	Clear Sky	0.5359	0.6984	0.5136	0.6733
	Partly cloudy	0.7041	0.8971	0.6957	0.7438
	Overcast	0.7826	0.8613	0.7984	0.7979
FAR	Clear Sky	0.2174	0.2431	0.1789	0.2016
	Partly cloudy	0.2959	0.1754	0.3107	0.2847
	Overcast	0.4641	0.2766	0.5543	0.3331

457  
 458 For the field identified as partly cloudy by the previous model, the random forest  
 459 cloud fraction model established in the preceding text is used to retrieve the cloud  
 460 fraction in the AGRI field. For samples classified as partly cloudy by the model, and

删除了: 83...0. Moreover, for some ...artly cloudy and overcast view fields, the possibilities of detection...OD is higher than those of ...perational cloud detection products. During nighttime, compared to operational cloud detection products, the LSTM...andom forest model increases the POD for clear sky from 0.51 to 0.73...7, with slightly ...igher possibilities of detection...OD for partia...y cloudy view fields compared tothan...the operational products, while the PODpossibility of detection...for full cloud...vercast view fields is lower. During the day, the Operational product has a lower false alarm rate...AR for clear sky compared to the LSTM...andom forest model, while the LSTM...andom forest model has a lower false alarm rate...AR for partly cloudy and overcast conditions compared tothan

删除了: Operational

删除了: LSTM...andom forest model significantly reduces the false alarm rate

格式化表格

删除了: LSTM

删除了: LSTM

删除了: Cloud Detection

删除了: Cloud Detection

删除了: 0.8294

删除了: 0.7341

删除了: 0.7223

删除了: 0.7101

删除了: 0.8435

删除了: 0.7523

删除了: 0.3633

删除了: 0.1983

删除了: 0.1677

删除了: 0.3488

删除了: 0.2358

删除了: 0.2105

删除了: For the view fields judged as partly cloudy by the



539 operational products, and 2B-CLDCLASS-LIDAR cloud fraction products, the mean  
 540 error and root mean square error (RMSE) of the cloud fraction retrieval were calculated  
 541 based on the matched 2B-CLDCLASS-LIDAR cloud fraction product as ground truth,  
 542 separately for daytime and nighttime operational cloud fraction products (columns 2  
 543 and 4) and the random forest- retrieved cloud fraction (columns 3 and 5), as shown in  
 544 Table 3. It can be observed that during daytime, compared to the FY-4A operational  
 545 cloud fraction product, the random forest cloud fraction retrieval model shows  
 546 significant improvement in both ME and RMSE. The ME decreases from 0.23 to 0.11,  
 547 and the RMSE decreases from 0.32 to 0.15, indicating that the random forest cloud  
 548 fraction retrieval model provides more accurate estimates of cloud fraction. For  
 549 nighttime, the ME of the operational cloud fraction product is positive, indicating an  
 550 overall overestimation of cloud fraction. In contrast, the ME of the random forest model  
 551 is negative, indicating an overall underestimation of cloud fraction. The RMSE of the  
 552 random forest model retrieval results during nighttime is lower than that of the  
 553 operational cloud fraction product.

554 **Table 3** Errors in cloud fraction retrieval

	Daytime Operational Product	Daytime <u>RF</u> Results	Nighttime Operational Product	Nighttime <u>RF</u> Results
ME	0.2374	0.1457	0.2488	-0.1984
RMSE	0.3269	0.2022	0.3374	0.2434

删除了: amount

删除了: amount

删除了: amount

删除了: amount

删除了: LSTM

删除了: inverted

删除了: amount

删除了: amount

删除了: LSTM

删除了: amount

删除了: mean error (

删除了:)

删除了: 19

删除了: LSTM

删除了: amount

删除了: amount

删除了: amount

删除了: amount

删除了: LSTM

删除了: amount

删除了: LSTM

删除了: amount

删除了: LSTM

删除了: LSTM

删除了: Cloud Detection

删除了: Cloud Detection

删除了: 1134

删除了: 1911

删除了: 1897

删除了: 2361

585 **3.2 Cloud fraction correction in sun glint regions**

586 Sun glint refers to the bright areas created by the reflection of sunlight to the  
587 sensors of observation systems (satellites or aircrafts). This phenomenon usually occurs  
588 on extensive water surfaces, such as oceans lakes or rivers. This specular reflection of  
589 sunlight will cause an increase in the reflected solar radiation received by onboard  
590 sensors, manifested as an enhancement of white brightness in visible images. The  
591 increase in visible channel observation albedo will affect various subsequent  
592 applications of data, including cloud detection and cloud cover retrieval, etc.

593 The position of Sun glint area can be determined using the SunGlintAngle value  
594 in the FY-4A GEO file. SunGlintAngle is defined as the angle between the satellite  
595 observation direction or reflected radiation direction and the mirror reflection direction  
596 on a calm surface (horizontal plane). It is generally accepted that the range of  
597 SunGlintAngle < 15° is easily affected by sun glint (Kay S, et al., 2009). The positions  
598 of the SunGlintAngle contour lines at 5 and 15° are marked in Figure 1(a). It can be  
599 observed that the edge of sun glint in Figure 1(a) essentially overlaps with the position  
600 of SunGlintAngle = 15°. Thus, the region where SunGlintAngle < 15° is defined as the  
601 sun glint range in this paper and only the cloud fraction within this range will be  
602 adjusted in the subsequent correction.

603 To correct the cloud fraction in the sun glint region, we initially identified 672  
604 fields of view where sun glint occurred in the FY-4A AGRI observations between 1

删除了: 2

删除了: 2

607 June and 31 July 2019. Subsequently, a direct least squares fitting was conducted  
608 between the retrieved cloud fraction and the collocated 2B-CLDCLASS-LIDAR cloud  
609 fraction (ground truth). The scatter plot is illustrated in Figure 1(b), where x-axis is the  
610 2B-CLDCLASS-LIDAR cloud fraction and y-axis is the model-retrieved cloud fraction.  
611 The blue line represents the curve (namely Eq. 2) fitted by the least squares method  
612 between the retrievals and the truths. The thin dash line is the  $x=y$  line. It is evident that  
613 the retrieved cloud fraction is generally slightly overestimated.

614 Taking observations at 04:00 on 5 June 2019 as an example, Figure 1(c) presents  
615 the distribution of SunGlintAngle and the flight trajectory of the Cloudsat&Calypso  
616 satellite. White circles denote the sun glint region with SunGlintAngle  $< 15^\circ$  and the  
617 white line represents the satellite flight track. As depicted in the figure, the majority of  
618 Cloudsat&Calypso flight trajectories do not pass through the central position of sun  
619 glint area but instead traverse locations with larger SunGlintAngle values. The  
620 intensity of sun glint effect decreases with the increase of SunGlintAngle. This  
621 suggests that the true values for spatial and temporal matching mostly do not fall within  
622 the strongest sun glint region. From Figure 1(d), it can be seen that the impact of sun

623 glint becomes stronger as SunGlintAngle decreasing, which results in a higher  
624 observation albedo. This further leads to the overestimated cloud fraction values in the  
625 retrieval. It is evident that the cloud fraction error is related to the value of  
626 SunGlintAngle and this influence is not considered in Eq. (2). Directly applying  
627 equation (2) to correct the cloud fraction retrievals would result in a too small correction

删除了: inverted

删除了: 2

删除了: inverted

删除了: 7

删除了: inverted

删除了: 2

删除了: 2

删除了: 7

删除了: 7

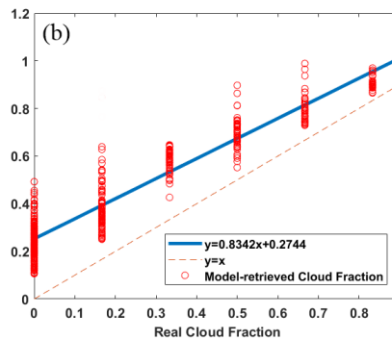
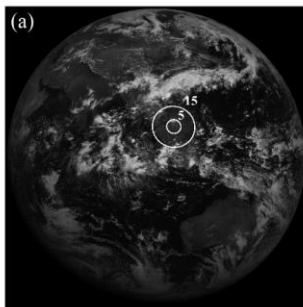
637 intensity for the FOVs near the center of sun glint and an excessively large correction  
 638 intensity for the FOVs in the Sun-glint edge region (even erroneous clear sky may  
 639 appear). Considering this, a correction formula (3)-(4) using SunGlintAngle as weight  
 640 is introduced, where  $W_i$  represents the angle weight for a certain pixel  $i$  in the sun glint  
 641 region,  $n$  is the number of pixels within the SunGlintAngle  $< 15^\circ$  range,  $y_i$  is the initial  
 642 model retrieval of cloud cover for the field of view  $i$  and  $x_i$  is the final corrected cloud  
 643 fraction.

644  $x = (y - 0.2744) / 0.8342$  (2)

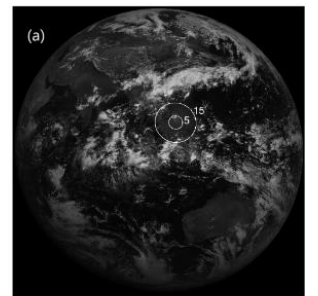
645  $W_i = \frac{\text{glintangle}_i}{\sum_{i=0}^n \text{glintangle}_i}$  (3)

646  $x_i = W_i \left( \frac{y_i - 0.2744}{0.8342} \right)$  (4)

647 Figure 1(d) shows the distribution of errors with respect to SunGlintAngle,  
 648 where the blue dots represent the error distribution corrected using formula  
 649 (2), and the orange dots represent the error distribution corrected using  
 650 formula (4). It can be seen from Figure 1(d) that after correction by formula  
 651 (4), the errors in the smaller range of SunGlintAngle are significantly reduced.



652



删除了: 8

删除了: 9

删除了: 2562

删除了: 8

删除了: 428

删除了: 7

删除了: 8

删除了: 2526

删除了: 8428

删除了: 9

删除了: 2

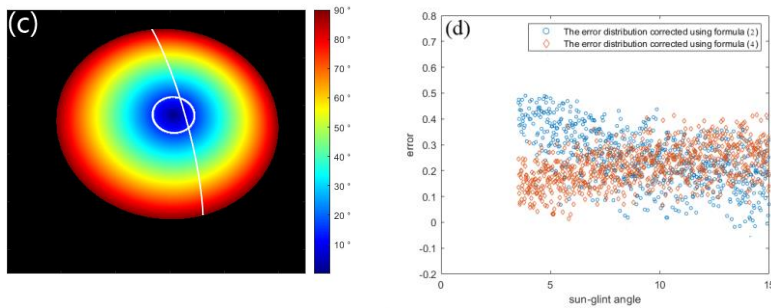
删除了: 7

删除了: 9

删除了: 2

删除了: 9

删除了:

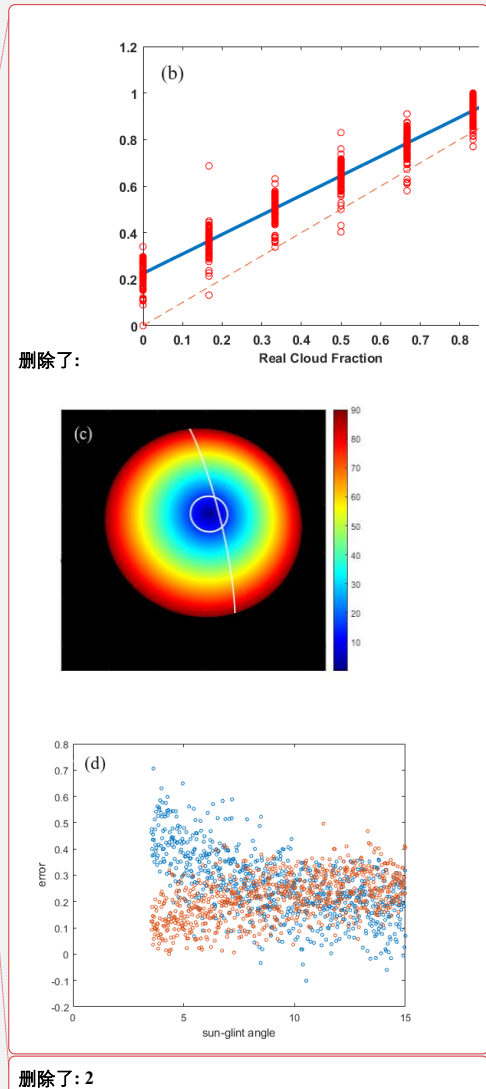


669  
 670 **Figure 1** (a) albedo image of 0.67 $\mu$ m channel (the circles are the contours of the sun-  
 671 glint angle), (b) Scatter plot of cloud fraction in sun glint region (The blue line  
 672 represents the curve (namely Eq.2) fitted by the least squares method between the  
 673 retrievals and the truths.), (c) Distribution of SunGlintAngle and satellite flight track of  
 674 CloudSat & Calypso at 4:00 on June 5, 2019, (d) Distribution of cloud fraction retrieval  
 675 error with sun-glint angle.

### 676 3.3 Algorithm universal applicability testing

677 Although the retrieval model in this article was built based on data from May 2019  
 678 due to the limited lifespan of the instrument, how effective is it in real-time FY-4A  
 679 AGRI observations and even subsequent FY-4B AGRI applications? The algorithm's  
 680 universal applicability was tested using real-time observations from FY-4A and FY-4B  
 681 AGRI in 2023.

682 Taking the full-disk observation of FY-4A AGRI at 04:00 (UTC, the same below)  
 683 on 1 June 2023 as an example, the radiance observations from 14 channels are initially  
 684 fed into the random forest cloud detection model to determine the sky classification



删除了:

删除了: 2

删除了: LSTM

690 (overcast, partly cloudy or clear sky) in each AGRI field. The random forest cloud  
691 fraction retrieval model is utilized to retrieve the cloud fraction in scenes identified as  
692 partly cloudy. Figure 2(a) is the observed albedo at 0.67  $\mu\text{m}$ , where the circles represent  
693 the contours of the sunlint angle, (b) is the cloud fraction retrievals from random forest  
694 algorithm, (c) is the official operational cloud fraction product and (d) is random forest  
695 cloud fraction retrievals with sun-glint correction. It can be seen from Figure 2 that  
696 many clear-sky scenes are erroneously identified as cloudy by the operational product  
697 and the cloud fraction is generally overestimated with many scenes having a cloud  
698 fraction of 1. The random forest algorithm identifies more regions as clear skies or  
699 partly cloudy than the operational products, matching better with the observations in  
700 the 0.67  $\mu\text{m}$  albedo image. Brighter regions in the visible image correspond to cloud  
701 cover areas and darker areas represent clear sky conditions. The sun glint region in the  
702 central South China Sea (the circled area in Figure 2(a)) is depicted in Figure 2(b),  
703 where the clear-sky scenes over the ocean are misidentified as partly cloudy by random  
704 forest algorithm due to the increase in observed albedo. Although operational product  
705 in this area also suffers from the impact of unremoved sun glint, it identifies more clear-  
706 sky scenes and the cloud fraction is relatively low. Thus, it is evident that the random  
707 forest algorithm exhibits significant cloud detection and cloud fraction errors in these  
708 sun glint regions. Correction is necessary for the cloud fraction retrievals in the sun  
709 glint region.

710 Figure 2(d) shows the cloud fraction distribution after correction using equation

删除了: LSTM

删除了: estimate

删除了: 3

删除了: LSTM

删除了: LSTM

删除了: 3

删除了: LSTM

删除了: 3

删除了: 3

删除了: LSTM

删除了: LSTM

删除了: 3

723 (9) in the sun glint region., The correction eliminates the influence of sun glint  
 724 comparing to the cloud fraction in sun glint area before correction in Figure 2(b). The  
 725 scenes misjudged as partly cloudy are corrected to clear sky and match well with the  
 726 actual albedo observations in 2(a), which accurately restores the true cloud coverage  
 727 over the South China Sea.

728

729

730

731

732

733

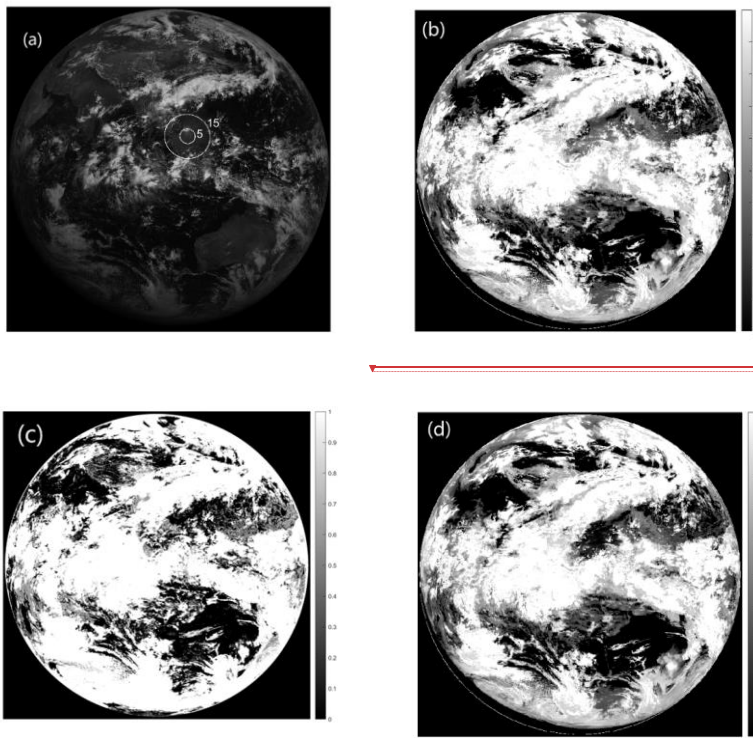


**Figure 2** FY-4A AGRI at 04:00 on 1 June 2023 (a) albedo image of 0.67 $\mu$ m channel (the circles are the contours of the sun-glint angle), (b) **random forest** cloud fraction retrieval without sun-glint correction, (c) operational cloud fraction product, (d)

删除了: 3

删除了: 3

删除了:

删除了:

删除了: 3

删除了: LSTM

740 random forest cloud fraction retrieval with sun-glint correction.

删除了: LSTM

741 Statistical analysis was conducted on the correction effect using samples with sun  
 742 glint in the training data. The POD and FAR in sun glint area is listed in table 4 and the  
 743 error is in table 5. The POD for clear skies has increased from 0.11 to 0.84. The FAR  
 744 for partly cloudy has decreased from 0.9 to 0.2. The mean error of cloud fraction  
 745 retrievals decreased from 0.398 to 0.136. These all indicate that the positive effect of  
 746 the sun glint correction.

删除了: possibility of detection...OD and false alarm rate...AR in sun glint area is listed in table 4 and the error is in table 5. The possibility of detection...OD for clear skies has increased from 0.09 ...1 to 0.83...4. The false alarm rate...AR for partly cloudy has decreased from 0.89 ... to 0.17.... The mean error of cloud fraction retrievals decreased from 0.176 ...98 to 0.09

747 **Table 4** POD and FAR of Cloud Detection in sun glint area

	Sky	Operational	<u>RF</u>	<u>RF after</u>
	Classification	Product		<u>Correction</u>
POD	Clear Sky	0.5535	0.1137	0.8443
	Partly cloudy	0.6738	0.8342	0.7677
	Overcast	0.8505	0.9498	0.9498
FAR	Clear Sky	0.1437	0.0120	0.2354
	Partly cloudy	0.3742	0.9077	0.2019
	Overcast	0.5545	0.0745	0.0745

删除了: The cloud mask recall rate

删除了: LSTM

删除了: LSTM after Correction

删除了: 0.0900

删除了: 0.8301

删除了: 0.8279

删除了: 0.7436

删除了: 0.9744

删除了: 0.9744

删除了: 0.0063

删除了: 0.3142

删除了: 0.8972

删除了: 0.1719

删除了: 0.1324

删除了: 0.1324

删除了: LSTM

删除了: LSTM

删除了: 0.2760

删除了: 0.1634

删除了: 0.1948

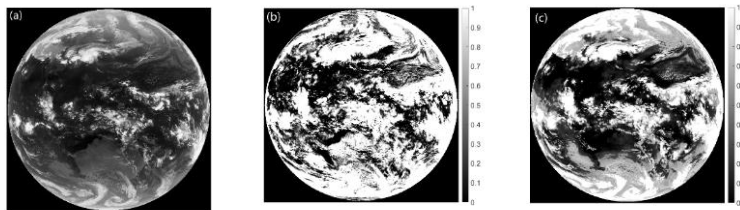
删除了: 0.1883

748  
 749 **Table 5** cloud fraction Errors in sun glint area

	Operational	Product	<u>RF</u> Retrievals	<u>RF after</u>
				<u>Correction</u>
ME	0.2691		0.3987	0.1365
RMSE	0.3458		0.3774	0.1639



811 FY-4B launched in 2021 has a total of 15 channels with an additional low-level  
 812 water vapor channel at 7.42  $\mu\text{m}$  compared to FY-4A. Taking the full-disk observation  
 813 of FY-4B AGRI at 17:00 on April 18, 2023, as an example, The radiance observation  
 814 data of the remaining eight channels (near-infrared and infrared channels) except for  
 815 the 7.42  $\mu\text{m}$  channel and the visible light channels were input into the random forest  
 816 cloud detection model. Figure 3 (a) shows the brightness temperature distribution  
 817 observed in the 10.8  $\mu\text{m}$  channel of FY-4B AGRI, (b) represents the operational cloud  
 818 fraction product for FY-4B AGRI and (c) shows the cloud fraction retrieved by this  
 819 algorithm. Figure 3 illustrates that the random forest algorithm identifies more regions  
 820 as clear skies or partly cloudy than the operational products, aligning better with the  
 821 brightness temperature observations in 10.8  $\mu\text{m}$ . Especially in high latitude regions of  
 822 the southern hemisphere and areas with strong convection near the equator, the cloud  
 823 cover provided by operational products is too high and even misjudged. It can be seen  
 824 that the random forest algorithm is also suitable for cloud fraction retrieval of FY-4B  
 825 AGRI.



826  
 827 **Figure 3** FY-4B AGRI at 17:00 on 18 April 2023, (a) brightness temperature of  
 828 10.8 $\mu\text{m}$  channel, (b) operational cloud fraction product, (c) random forest cloud

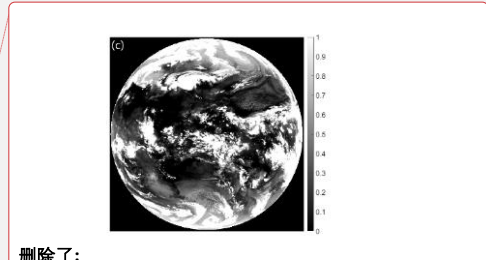
删除了: LSTM

删除了: 4

删除了: 4

删除了: LSTM

删除了: LSTM



删除了:

删除了: 4

删除了: LSTM

837 fraction retrieval.

838

#### 839 4 Conclusion

840 The random forest machine learning algorithm based on FY-4A AGRI full-disc  
841 level-1 radiance observations is developed to retrieve the cloud fraction for each field  
842 of view in this paper. The accuracy of the algorithm is validated using the 2B  
843 CLDCLASS-LIDAR cloud fraction product from the Cloudsat&Calypso active remote  
844 sensing satellite and FY-4A AGRI level 2 operational product. The following  
845 conclusions are drawn:

846 (1) Not only the cloud detection but also the cloud fraction within each FY-4A

847 AGRI field of view can be retrieved by the random forest machine learning  
848 algorithm.

849 (2) The operational product has a relatively low POD for clear sky scenes, while  
850 the random forest algorithm improves the POD for clear sky scenes during the  
851 daytime from 0.54 to 0.69. The POD for clear sky scenes at night increases  
852 from 0.51 to 0.67, and the POD for partly cloudy and overcast scenes is  
853 comparable to the operational product.

854 (3) For partly cloudy fields, during the day, the ME and RMSE of the operational  
855 product are 0.2374 and 0.3269, respectively, while this algorithm exhibits

删除了: long short-term memory (LSTM

删除了:)

删除了: LSTM

删除了: high

删除了: false alarm rate

删除了: LSTM

删除了: probability of detection (

删除了: )

删除了: 83

删除了: However, the false alarm rate (FAR) is higher compared to the operational product.

删除了: 73

删除了: ial

删除了: fully cloudy

删除了: mean error

删除了: root-mean-square error

872 lower ME (0.1475) and RMSE (0.2022) compared to the operational product.

873 At night, the operational product tends to overestimate cloud cover, while this

874 algorithm underestimates cloud cover, with a lower RMSE compared to the

875 operational product.

876 (4) The cloud fraction correction curve for sun glint region fitted with

877 SunGlintAngle as weight significantly improves the accuracy of the random

878 forest cloud fraction retrievals. It reduces the misjudgment rate where increased

879 albedo leads to the identification of clear-sky scene as partly cloudy or overcast.

880

#### 881 *Data availability*

882 FY-4A AGRI data is available at <http://satellite.nsmc.org.cn> and the 2B-CLDCLASS-

883 LIDAR data at <https://www.icare.univ-lille.fr/data-access/data-archive-access/>

884

#### 885 *Author contributions*

886 JX: Formal analysis, Methodology, Software, Visualization and Writing – original draft

887 preparation. LG: Conceptualization, Data curation, Funding acquisition, Supervision,

888 Validation and Writing – review & editing.

889

#### 890 *Competing interests*

891 The contact author has declared that none of the authors has any competing interests.

892

删除了: mean error

删除了: 1134

删除了: 1897

删除了: than

删除了: LSTM

898 **Disclaimer**

899 **Acknowledgements**

900 Funding: This work was supported by the National Natural Science Foundation of

901 China under grant no. 41975028.

902 [We acknowledge the High Performance Computing Center of Nanjing University of](#)

903 [Information Science & Technology for their support of this work.](#)

904 **References**

905 [Baum, B., Trepte Q.: A Grouped Threshold Approach for Scene Identification in](#)

906 [AVHRR Imagery, \*Journal of Atmospheric & Oceanic Technology\*, 16, 793-800,](#)

907 [https://doi.org/10.1175/1520-0426\(1999\)016<0793:AGTAFS>2.0.CO;2](https://doi.org/10.1175/1520-0426(1999)016<0793:AGTAFS>2.0.CO;2), 1999.

908 [Breiman L.1999. Random Forests-Random Features \[J\]. \*Machine Learning\*.45\(1\): 5-32.](#)

909 Merchant, C.J., Harris, A.R., Maturi, E., Maccallum S.: Probabilistic physically based

910 cloud screening of satellite infrared imagery for operational sea surface temperature

911 retrieval, *Quarterly Journal of the Royal Meteorological Society*, 131, 2735-2755,

912 <https://doi.org/10.1256/qj.05.15>, 2005.

913 Gao, J., Jing, Y.: Satellite Remote Sensing Cloud Detection Method Based on Fully

914 Convolutional Neural Network,*Infrared Technology*, 41, 607-615, 2019.

915 Gomez-Chova, L., Camps-Valls, G., Amoros-Lopez, J., Guanter, L., Alonso, L.,

916 Calpe, J., Moreno, J.: New Cloud Detection Algorithm for Multispectral and

917 Hyperspectral Images: Application to ENVISAT/MERIS and PROBA/CHRIS

删除了: Bai, S., Shen, X.: PM2.5 prediction based on LSTM recurrent neural network, *Computer Applications and Software*, 36, 67-70, 2019.

Bao S., Qin H., Dai Y.: Short-term precipitation prediction research based on UI-LSTM model, *Radio Engineering*. 1-10, 2023.

924 Sensors, *IEEE International Symposium on Geoscience and Remote Sensing*, 2757–  
925 2760, doi:10.1109/igarss.2006.709, 2006.

926 Hu, J.: Research on Cloud Detection Algorithm of Remote Sensing Image Based on  
927 Convolution Neural Network, *Nanjing University of Information Science and*  
928 *Technology*, doi:10.27248/d.cnki.gnjqc, 2020.

929 Kay, S., Hedley, J., Lavender, S.: Sun Glint Correction of High and Low Spatial  
930 Resolution Images of Aquatic Scenes: a Review of Methods for Visible and Near-  
931 Infrared Wavelengths, *Remote Sensing*, 1, 697-730,  
932 <https://doi.org/10.3390/rs1040697>, 2009.

933 Kegelmeyer, W.P.J.: Extraction of cloud statistics from whole sky imaging  
934 cameras, 1994.

935 Kong, Y.-L., Huang, Q., Wang, C., Chen, J., Chen, J., & He, D. (2018). Long Short-  
936 Term Memory Neural Networks for Online Disturbance Detection in Satellite  
937 Image Time Series. *Remote Sensing*, 10(3), 452. doi:10.3390/rs10030452

938 [Mace, G. G., R. Marchand, Q. Zhang, et al. \(2007\). CloudSat Project: Level 2 Radar-](#)  
939 [Lidar GEOPROF product process description and interface control document. Jet](#)  
940 [Propulsion Laboratory.](#)

941 Pan, C., Xia B., Chen, Y.: Research on MODIS Cloud Detection Algorithms Based on  
942 Fuzzy Clustering, *Microcomputer Information*, 25, 124-125+131, 2009.

943 [Quesada-Ruiz L C, Rodriguez-Galiano V F, Zurita-Milla R, et al. 2022. Area and](#)  
944 [Feature Guided Regularised Random Forest: a novel method for predictive](#)

删除了: Li, W., Zhang, L., Chen, X., Li, D.: The universal cloud detection algorithm of MODIS data, *Society of Photo-Optical Instrumentation Engineers (SPIE) Conference Series*, 64190F-64190F-6, doi:10.1117/12.712722, 2006.

949 [modelling of binary phenomena. The case of illegal landfill in Canary Island \[J\].](#)

950 [International Journal of Geographical Information Science, 36\(12\): 2473-2495.](#)

951 Rossow, W. B., Leonid, C.G.: Cloud detection using satellite measurements of  
952 infrared and visible radiances for ISCCP. *Journal of Climate*, 12, 2341-2369,  
953 [https://doi.org/10.1175/1520-0442\(1993\)006<2341:CDUSMO>2.0.CO;2](https://doi.org/10.1175/1520-0442(1993)006<2341:CDUSMO>2.0.CO;2), 1993.

954 [Solvsteen, C.: Correlation based cloud-detection and an examination of the split-](#)  
955 [window method, \*Proceedings of SPIE - The International Society for Optical\*](#)  
956 [Engineering](#), 86-97, 1995.

957 Amato, U., Antoniadis, A., Cuomo, V., Cutillo, L., Franzese, M., Murino, L., Serio,  
958 C.: Statistical cloud detection from SEVIRI multispectral images, *Remote Sensing*  
959 *of Environment*, 112, 750–766, <https://doi.org/10.1016/j.rse.2007.06.004>, 2008.

960 Wang, Z.: CloudSat Project: CloudSat 2B-CLDCLASS-LIDAR product process  
961 description and interface control document, *Jet Propulsion Laboratory*, 2019.

962 Yan, J., Guo, X., Qu, J.: An FY-4A/AGRI cloud detection model based on the naive  
963 Bayes algorithm, *Remote Sensing for Natural Resources*, 34, 33-42, 2022.

964 Zhang, W., He, M., Mak, M.W.: Cloud detection using probabilistic neural networks,  
965 *Geoscience and Remote Sensing Symposium*, IEEE 2373-2375, 2001.

966 Zhang, Y., William, B. R., Andrew, A. L., Valdar, O., Michael, I. M.: Calculation of  
967 radiative fluxes from the surface to the top of atmo- sphere based on ISCCP and  
968 other global data sets: Refine- ments of the radiative transfer model and the input  
969 data, *Journal of Geophysical Research Atmospheres*, 109, 1-27,

删除了: Sarkar, V.: Optimized Unrolling of Nested Loops,  
*International Journal of Parallel Programming*, 29, 545-  
581, <https://doi.org/10.1023/A:1012246031671>, 2001.

973 <https://doi.org/10.1029/2003JD004457>, 2004.

974

删除了: Zhang, Y., Yang, C., Tao, R.: Multi-temporal Cloud Detection Method for Qin-ghai-Tibet Plateau based with FY-4A Data, *Remote Sensing Technology and Application*, 35, 389-398, 2020.  
Zhen, J., Liu, D., Wang Z.: Analysis of global distribution and seasonal variation characteristics of clouds using CloudSat/CALIPSO satellite data, *Meteorological Journal*, 76, 420-433, 2018.